The Spatial Distribution of Charge Exchange Loss Contributions to Storm Time Ring Current Decay: Van Allen Probes Observations

S. Y. Li[1,2,3], H. Luo[1,2,3,*], Y.S. Ge[1,2,3], A.M. Du[1,2,3,4], E. A. Kronberg[5], C. Huang[1,2,3], Y. Zhang[1,2,3], G.X. Chen[1,2,3]

[1]Key Laboratory of Earth and Planetary Physics, Institute of Geology and Geophysics, Chinese Academy of Sciences, Beijing, 100029, China

[2]Geoscience school, University of Chinese Academy of Sciences, Beijing, 100049, China

[3]Innovation Academy for Earth Science, CAS, Beijing, 10029, China

[4]Macau University of Science and Technology, Macau, China

[5]Department of Earth and Environmental Sciences, Ludwig-Maximilians University, Munich, Germany

Key words: charge exchange loss; ring current decay; Van Allen Probes

*Hao Luo (Corresponding author) luohao06@gmail.com

Abstract: Charge exchange between hot ions and cold neutral atoms is an important effect in ring current loss processes on magnetized planets. In this letter, we investigate the spatial distribution of charge exchange loss contributions to terrestrial ring current decay using data from the Van Allen Probes. These contributions were calculated by dividing local energetic neutral atom energy density escape rates by local ring current energy density decay rates. The results exhibit clear MLT and L dependence, with larger contributions observed nightside during the recovery phase of geomagnetic storms. The contribution of H^+ peaked at L~4 during early recovery phases and was stronger at higher L shells during late recovery phases, while O^+ decreased slightly with L shell. Possible explanations for this inhomogeneous distribution are also discussed. The asymmetric exospheric hydrogen density distribution may cause the inhomogeneous distribution in the MLT, while the L dependence may be related to the charge exchange cross-section and the ion energy flux. These results provide the first spatial distribution of charge exchange contributions, which is helpful for understanding local terrestrial ring current evolution.

1. Introduction

A critical part of the global system on most magnetized planets (e.g., Earth, Jupiter, and Saturn) involves a current carried by magnetospheric charged particles flowing in the azimuthal direction near the equatorial plane, often referred to as the “ring current” (Sergis et al., 2018). The terrestrial ring current consists of ions with energies ranging from a few keVs to several hundred keVs, flowing toroidally around the Earth at distances of roughly 2-8 R_E (Daglis et al., 1999). Severe perturbations can be induced in

this ring current by solar winds, called geomagnetic storms (Gonzalez et al., 1994). On Jupiter, injection-like phenomena caused by solar winds can occur in clusters, called "energetic events" (Louarn et al., 2000), that are likened to magnetic storms on Earth (Mauk et al., 1999). Similar particle injections also occur on Saturn (Mauk et al., 2005). The addition and loss of ions is critical to the evolution of ring currents on most magnetized planets.

Charge exchange is a common loss process for magnetized planets. On Earth, charge exchange between the ring current energetic ions and cold neutral hydrogen from the exosphere have been assumed to be the primary contributors to storm time terrestrial ring current degradation (Daglis & Kozyra, 2002; Fok et al., 1993; Jorgensen et al., 2001; Keika et al., 2006). On Saturn, charge exchange occurs between hot ring current ions and cold neutral gases from Enceladus (Mauk et al., 2005). On Jupiter, cold neutral atoms originate from gases sputtered by Io (Mauk, 2020; Smith et al., 2019) and Euorpa at R = 9.5 R_J (Mauk, 2004; Mauk et al., 2003).

Additional loss processes proposed on Earth include: precipitation into the ionosphere due to pitch angle scattering by electromagnetic ion cyclotron (EMIC) waves (Jordanova et al., 2006; Jorgensen et al., 2001) or by field line curvature (FLC) (Ebihara et al., 2011; Young et al., 2008), outflow of energetic ions from the magnetosphere through the magnetopause (Keika et al., 2005; Liemohn et al., 2001), and Coulomb collisions between hot ring current ions and plasmaspheric electrons (Fok et al., 1995). On Jupiter and Saturn, losses are also associated with scattering by waves of particles into the loss cone (Mauk, 2020).

While various loss mechanisms have been proposed, few studies have statistically investigated the spatial dependence of loss process contributions, which could provide valuable insights into the different roles of loss processes at specific spatial positions. As such, in the present study, we estimate local charge exchange energy losses for the terrestrial ring current (H^+ and O^+) and statistically examine their contributions to local current decay. Charge exchange loss is typically measured by energetic neutral atoms (ENAs), which are products of charge exchange processes (Fahr et al., 2007; Wing et al., 2020). ENAs are no longer trapped by the magnetic field, carrying significant amounts of energy escaping from the magnetosphere, thereby reducing the energy of ring currents on magnetized planets (Cheng, 1986; Keika et al., 2006; Mauk et al., 2003). ENA energy was simulated in this study using the model of Keika et al. (2011), based on differential ion flux data from the Van Allen Probes. To the best of our knowledge, this is the first statistical investigation of the spatial distribution of charge exchange loss contributions for both H^+ and O^+.

2. Data and methodology

2.1 Data

This study utilized ion data (Level 3) from the RBSPICE and HOPE instruments onboard the Van Allen Probes, which consist of two sun-pointing, spin-stabilized spacecrafts (A and B) in a highly elliptical, 9-hour, near-equatorial orbit with perigee at 1.1 R_E and apogee at 5.8 R_E. The HOPE (Funsten et al., 2013) and RBSPICE (Mitchell et al., 2014) instruments provide measurements of ion flux (H^+ and O^+) with energies of 1–50 keV and >50 keV, respectively. RBSPICE provides measurements of

oxygen ions without differentiating charge states, but O^+ should dominate. The data products we used from the RBSPICE instrument include: PAP_TOF × EH and PAP_TOF × EO products acquired from the TOF × E measurements, and PAP_TOF×PHOHELT data obtained from the TOF×PH measurements. The TOF×E products included H^+ ion flux with energies of 55–600 keV and O^+ data for the 183–665 keV range, while the TOF×PH products included O^+ ion flux with energies of 53–169 keV. The type of the ion fluxes we used was the omni-directional differential ion flux observed for each energy channel. All HOPE data were multiplied by 2 to match the RBSPICE measurements. The cross-calibration of these instruments is detailed on the LANL website (http://rbsp-ect.lanl.gov/rbsp_ect.php), wherein 87% of the data points agree to within a factor of 2 for protons on RBSPs. The spacecraft orbit completely covered the MLT and L range (L=3–5.5) between January 2013 and December 2016, making the data appropriate for spatial distribution studies.

The observation period exhibited 18 magnetic storms with an SYM-H index minimum smaller than −100nT and 61 storms with an SYM-H index minimum between −100nT and −50nT. Each storm was analyzed visually and the start (minimum of the SYM-H index) and end (up to pre-storm level, no less than -20nT) times for the recovery phase were recorded. Early and late recovery phases were divided visually using the SYM-H index recovery rate, when the slope changed significantly.

2.2 Methodology

Local charge exchange energy loss rates were estimated using simulated ENAs calculated using the modified method of Keika et al. (2006; 2011). In these studies, the

distribution was assumed to be isotropic and the total ENA energy escaping from the spherical surface per unit time $(\frac{dQ}{dt})$ was given by:

$$\frac{dQ}{dt} \approx 4\pi \sum_i E_i \Delta E_i \int \sigma_i^{10} n_H J_i^{ION} dV , \quad (1)$$

In our study, we assumed the spherical surface was infinitely small at the observed position of interest. The corresponding ENA energy density escape rate was then:

$$\frac{dD}{dt} \approx 4\pi \sum_i E_i \Delta E_i \sigma_i^{10} n_H J_i^{ION} , \quad (2)$$

where σ^{10} is the charge-exchange cross section calculated by Lindsay and Stebbings (2005), n_H is the geocorona density calculated by Rairden et al. (1986) and Cson Brandt et al. (2002), J^{ION} is the omni-directional differential flux of ions from the Van Allen Probes observations, and $E_i(\Delta E_i)$ is the geometrical mean energy (the energy band width) of the i^{th} energy step.

Ring current energy density decay rate at the observation point was calculated as the decrease in energy density between two adjacent sampling points divided by the sampling interval. Energy density was given by:

$$\varepsilon = 2\pi \sum_i \sqrt{2mE_i} J_i^{ION} \Delta E_i , \quad (3)$$

The differential mean value theorem suggests the decay rate can be replaced by:

$$\frac{\varepsilon(t_2) - \varepsilon(t_1)}{t_2 - t_1} = \varepsilon'(t) \qquad t \in (t_1, t_2) , \quad (4)$$

where $\varepsilon(t_1)$ and $\varepsilon(t_2)$ are the calculated energy densities at two adjacent sampling points and $\varepsilon'(t)$ is the slope of a linear fit to the data. The window length for this fit is 7.5 minutes, during which the distance traveled by the probes did not exceed 0.2 MLT×0.2 L.

The results of equation (4) included both spatial variations for the spacecraft and temporal variations. Thus, to exclude the effects of orbital displacement, a correction was made using average energy density variations with L shell, from the RBSP data (observed in the L shell from 2013 to 2016). Four calibration curves were used for specific geomagnetic conditions, including: SYM_H < −50 nT, −50 nT < SYM_H < −30 nT, −30 nT < SYM_H < −10 nT, and SYM_H > −10 nT. The calibration curve was subtracted from the change in energy density only if the change in the L shell exceeded 0.001 L in a 30s window. A detailed description of this correction process is provided in the Appendix.

Finally, we can determine the charge exchange loss contribution at any given location by dividing the ENA energy density escape rate by the ring current energy density decay rate.

3. Results

A case study from an April 11–17 (2014) storm is shown in **Figure 1**, to illustrate the calculation of charge exchange contributions. A period of 1.5 hours was selected during the early recovery phase, as indicated by the two black lines in **Figure 1a.** **Figures 1b-1f** show corresponding results for this period. The SYM_H index increases with time during the recovery phase of the storm, while the energy density decreases, as shown in **Figure 1c**. **Figure 1d** displays the change rate for the energy density. The blue line represents the change for two adjacent sampling points, divided by the sampling interval. The red line shows the two-step correction to the blue line results. First, the slope of a linear fit line was used to replace the blue line result, as shown in Equation

(4). Second, changes in energy density caused by variations in spacecraft location were subtracted using the calibration curve, according to the instantaneous SYM-H index for each observed time. This produced the corrected energy density decay rate (the red line result).

The charge exchange energy density loss rate (ENA energy density escape rate), calculated using Equation (2), is shown in **Figure 1e**. The blue and red lines correspond to H^+ and O^+, respectively. **Figure 1f** shows the charge exchange loss contribution, calculated by dividing the result of **Figure 1e** by that of **Figure 1d**. It is evident the charge exchange contribution of H^+ is higher than that of O^+. In addition, the satellite orbit during this period is at 11–13 MLT (the area with the lowest charge exchange contribution), as seen in the statistical results of **Figure 3c**.

The spatial distributions of the results for each charge exchange contribution calculation step, during the storm recovery phase from January 2013 to December 2016, were investigated statistically. The results are provided in polar MLT-L coordinates in **Figure 2**. The equatorial plane was divided into 0.5MLT×0.5L grids, in which the color represents an average over all points in the grid. The Spatial distributions of ENA energy density escape rates, calculated using Equation (2) for H^+ and O^+ during the early recovery phase, are shown in **Figures 2a** and **2b**, while those of the late recovery phase are shown in **Figures 2e** and **2f**. Note the ENA energy density escape rate is larger at nightside than at dayside for both H^+ and O^+. In addition, the O^+ rate is larger at lower L shells, while that of H^+ is largest at L~4. **Figures 2c** and **2g** show spatial energy density distributions in agreement with previous studies (Daglis et al., 2003; Ebihara &

174 Ejiri, 2000; Fok et al., 1996; Le et al., 2004; Liemohn et al., 2001). Ring current energy
175 density is asymmetric during the early recovery phase, as shown in **Figure 2c**, but its
176 MLT distribution becomes symmetric in late recovery phases, as shown in **Figure 2g**.
177 However, the decay rate MLT distributions are nearly symmetric throughout the
178 recovery phase, as shown in **Figures 2d** and **2h**, with larger values at lower L shells.

179 **Figure 3** shows the spatial distribution of charge exchange energy density loss rate
180 contributions (percentages) to local ring current energy density decay rates for both H^+
181 and O^+. **Figures 3a-3d** and **3e-3h** show statistical results from early and late recovery
182 phases, respectively. The results exhibit a clear MLT dependence for both H^+ and O^+,
183 with larger values appearing at nightside, similar to the distribution of ENA energy
184 density escape rates shown in **Figure 2**. We estimated the average global charge
185 exchange contribution for H^+ (O^+) at nightside to be nearly twice as large as that at
186 dayside in the early recovery phase and ~2.5 times larger in the late recovery phase.
187 This day-night asymmetry is consistent with the day-night asymmetry in the model
188 result for the exospheric hydrogen density distribution (Cson Brandt et al., 2002;
189 Rairden et al., 1986), as shown in **Figure 4g**.

190 Average charge exchange contributions from H^+ and O^+ are shown for varying L
191 shells ($\Delta L = 0.25$) in **Figures 3d** and **3h**. Vertical error bars indicate statistical errors,
192 indicated by the standard deviation of all points in each grid. The blue and orange
193 rectangles correspond to the error bars for H^+ and O^+, respectively. **Figure 3d** shows a
194 peak in the average charge exchange contribution from H^+ at L=4. The average
195 contribution from O^+ decreases monotonically with L shell during the early recovery

196 phase. In **Figure 3h**, the H^+ average contribution increases monotonically with L shell
197 but the growth rate decreases when L>5 during the late recovery phase. The overall
198 trend for O^+ is consistent across both phases.

199 **Figure 3** also clearly indicates the charge exchange contribution from H^+ is larger
200 than that of O^+. We estimated the average global charge exchange contribution from H^+
201 to be twice as large as that of O^+ in the early recovery phase and nearly 3 times larger in
202 the late recovery phase, suggesting H^+ is more dominant than O^+ in energy loss
203 processes. In addition, the average contribution from O^+ during the early recovery
204 phase was ~1.5 times larger than that during the late phase. This is consistent with the
205 results of Keika et al. (2006), who showed that O^+ charge exchange contribution
206 increased as Dst index decreased. Similar studies (Daglis et al., 2003; Hamilton et al.,
207 1988) have also demonstrated that O^+ was important in early rapid recovery phases.

208 # 4. Discussion

209 The L dependence of charge exchange contributions shown in **Figure 3** was
210 investigated by examining average charge exchange cross-section and average ion
211 energy flux varying with L shell. These important factors were calculated using H^+ and
212 O^+ data from the Van Allen Probes, collected from 2013 to 2016. The average ion
213 energy (**Figures 4a-4b**), cross-section (**Figures 4c-4d**), and energy flux (**Figures 4e-4f**)
214 were plotted as functions of L shell ($\Delta L = 0.25$) during both early and late recovery
215 phases. **Figure 4g** shows the exospheric hydrogen density distribution calculated using
216 the model of Cson Brandt et al. (2002) and Rairden et al. (1986). The blue and red
217 lines represent early and late recovery phases, respectively. Average ion energy shown

in **Figures 4a-4b** was given by:

$$\bar{E}_{Ion} = \frac{\sum_i E_i \Delta E_i J_i^{Ion}}{\sum_i \Delta E_i J_i^{Ion}}, \quad (5)$$

where J^{ION} is the omni-directional differential ion flux and $E_i(\Delta E_i)$ is the geometrical mean energy (the energy bandwidth) of the i^{th} energy step. The model of Lindsay and Stebbings (2005) was then used to calculate average charge exchange cross-sections for H^+ and O^+ using average ion energy data, as shown in **Figures 4c-4d**.

The H^+ cross-section increases monotonically with L shell while the growth rate decreases for L>4. The average energy flux for H^+ (shown in **Figure 4e**) was calculated from the differential ion flux observed by the Van Allen Probes. It peaks at L~4, which is consistent with the results of previous studies (Keika et al., 2011; McEntire et al., 1985). These results suggest contributions should increase monotonically with L shell throughout the recovery phase. However, a decrease occurs in the early recovery phase (L>4) because of a rapid decrease in average energy flux. A gradual flux decrease occurs in late recovery phases (L>4), which did not reverse the trend of increasing charge exchange contributions due to larger cross-section. However, this effect is sufficient to limit flux increasing for L>5. Thus, we can infer that although the cross-section is an important factor in the L-dependence of H^+ charge exchange, energy flux becomes a dominant factor for L>4.

Average charge exchange cross-sections for O^+ are observed to decrease monotonically with L shell throughout the recovery phases, as shown in **Figure 4d**, which is consistent with the L dependence of O^+ contributions. In other words, the

cross-section, not the energy flux, is the dominant factor in O^+ charge exchange. In addition, contributions from O^+ are slightly larger than those of H^+ at L=3–3.5, as seen in **Figures 3d** and **3h**. Cross-section is also a dominant factor for H^+ at L<4 and is 2–3 orders of magnitude smaller than that of O^+ at L=3–3.5, as shown in **Figures 4c** and **4d**, suggesting contributions from O^+ are larger than those of H^+.

Figure 3 shows a clear MLT dependence of the charge exchange contribution, including a day-night asymmetry caused by similar trends in exospheric hydrogen density distributions, calculated using the model of Rairden et al. (1986) and Cson Brandt et al. (2002). Ilie et al. (2013) determined the neutral hydrogen density distribution in the equatorial plane using various geocoronal models, most of which (Bailey & Gruntman, 2011; Østgaard, 2003; Zoennchen et al., 2010) also predicted a day-night asymmetry. Cson Brandt et al. (2002) compared two exospheric models (day-night symmetric and asymmetric), achieving more realistic plasma sheet flux with a model exhibiting higher nightside exospheric hydrogen densities. Thus, day-night asymmetry in the exospheric hydrogen density distribution may be the most plausible explanation for the similar trend in charge exchange.

5. Conclusions

In summary, this study presents the first statistical survey of charge exchange contribution spatial distributions for both hydrogen and oxygen ring current ions. Several conclusions are presented below. 1) A clear spatial dependence was observed. The MLT dependence of both H^+ and O^+ exhibited larger charge exchange contributions nightside throughout the recovery phase. For the L dependence, there was

a peak H^+ contribution at L~4 during the early recovery phase, while the contribution increased monotonically with L shell but the growth rate became small for L>5 during the late recovery phase. The O^+ contributions decreased monotonically with L shell throughout the recovery phase. 2) The contribution of H^+ was more dominant than that of O^+ in the charge exchange energy loss process.

Our study provides valuable insights into the role of charge exchange loss processes at different spatial positions, which is helpful for understanding local terrestrial ring current evolution. We believe that contributions from the other three terrestrial ring current decay mechanisms, introduced in **Section 1**, are also important. Their contributions to ring current decay may also be spatially asymmetric, as with the charge exchange process. However, a study of these effects is beyond the scope of this paper and is expected to be studied in a future work.

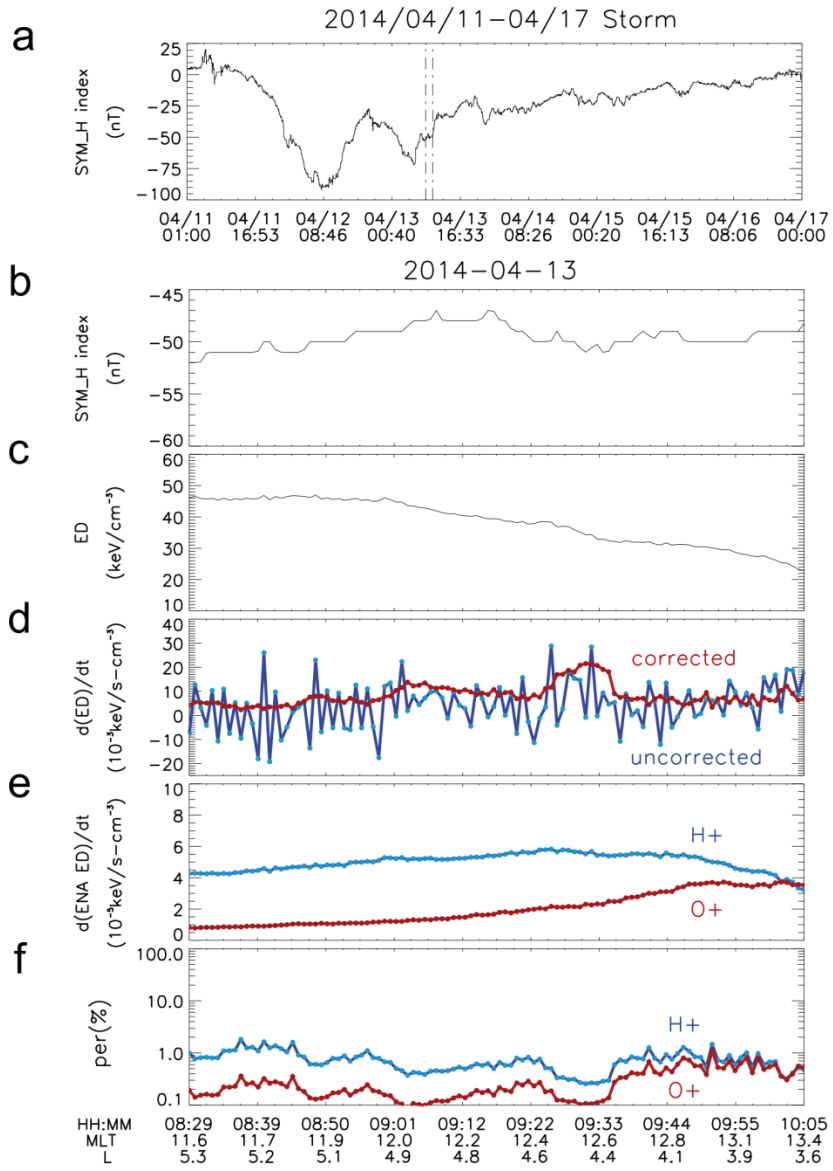

Figure 1. (a) The SYM_H index during an April 11–17 (2014) storm. (b)-(f) Plots during the time indicated by the two black dashed lines in Figure 1a. (b) SYM_H index. (c) Local ring current energy density sums for H^+ and O^+, calculated using Equation (3). (d) The initial result (blue line) and corrected result (red line) for ring current energy density decrease rate. (e) ENA energy density escape rates for H^+ (blue line) and O^+ (red line), calculated using Equation (2). (f) The contribution (percentage) of ENA energy density escape rate to the corrected ring current energy density decrease rate for H^+ (blue line) and O^+ (red line).

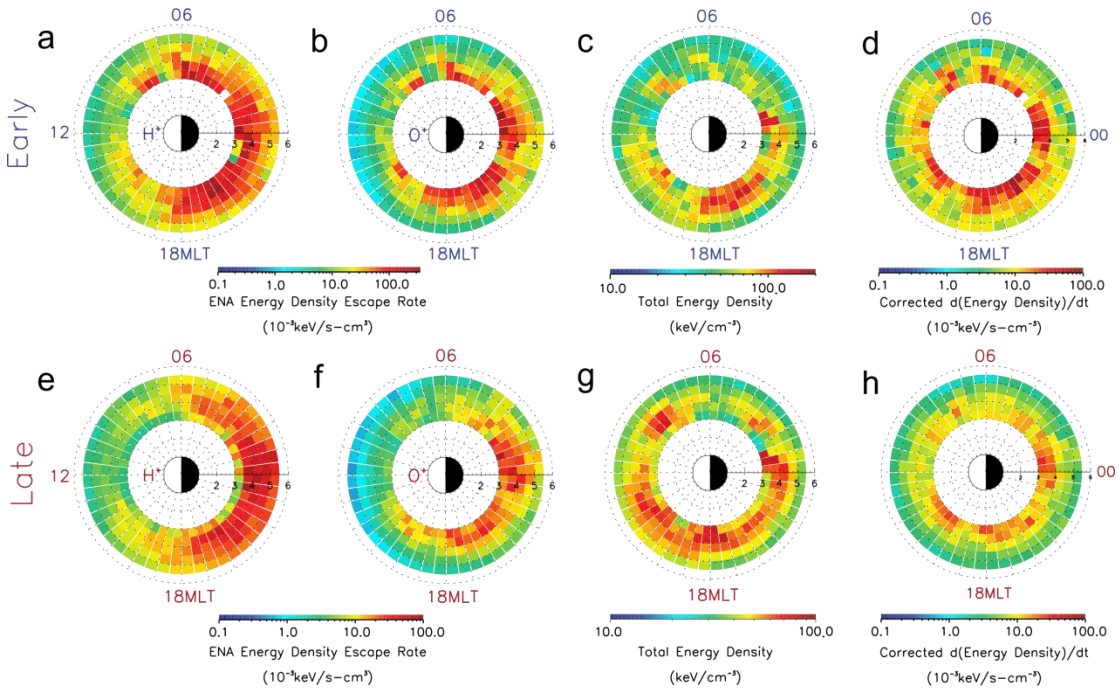

Figure 2. An overview of spatial distribution results during an early (a)-(d) and late (e)-(h) recovery phase. (a), (b), (e), (f) ENA energy density escape rates for H^+ and O^+. (c), (g) Ring current energy density sums for H^+ and O^+, calculated using Equation (3). (d), (h) Corrected ring current energy density decay rates. All results are shown in polar MLT-L coordinates and the value in each grid (0.5MLT×0.5L) is an average over all points in the grid.

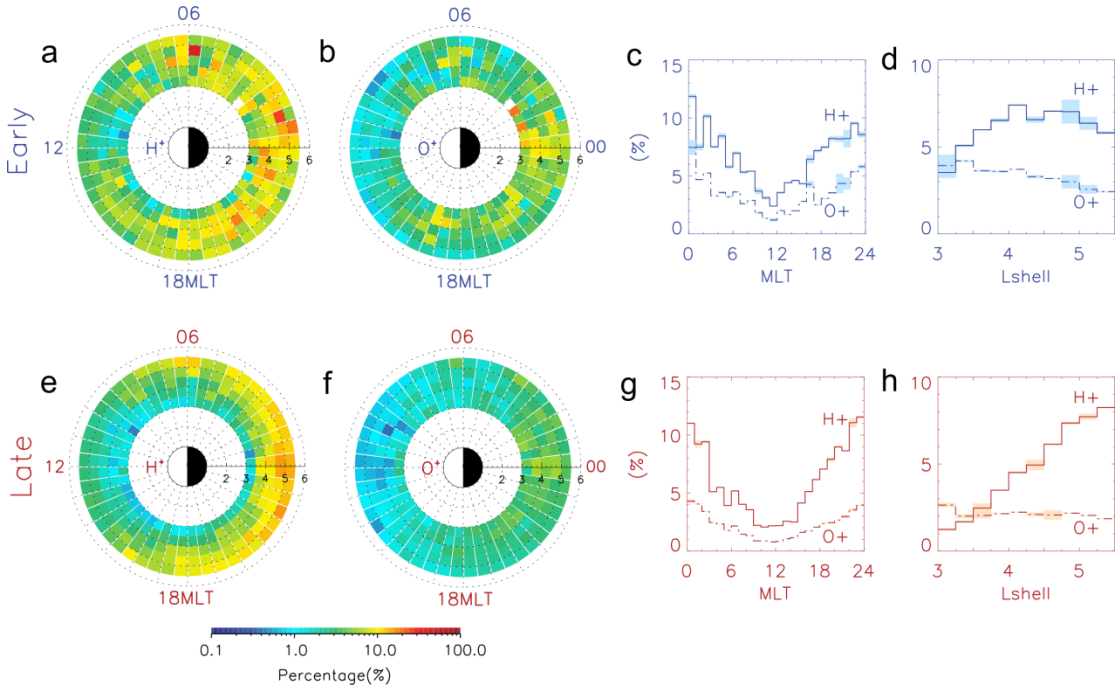

Figure 3. The spatial distribution of charge exchange energy density loss rate contributions to local ring current energy density decay rates, for H^+ and O^+, during early (a)-(d) and late (e)-(h) recovery phases. (a), (b), (e), (f) Spatial distributions in polar MLT-L coordinates. The other format is equivalent to that of Figure 2. (c), (g) Average contributions for H^+ (solid lines) and O^+ (dashed lines) as a function of MLT (ΔMLT=1). (d), (h) Average contributions as a function of L shell ($\Delta L = 0.25$). The error bars for early (late) recovery phases are denoted by blue (orange) rectangles.

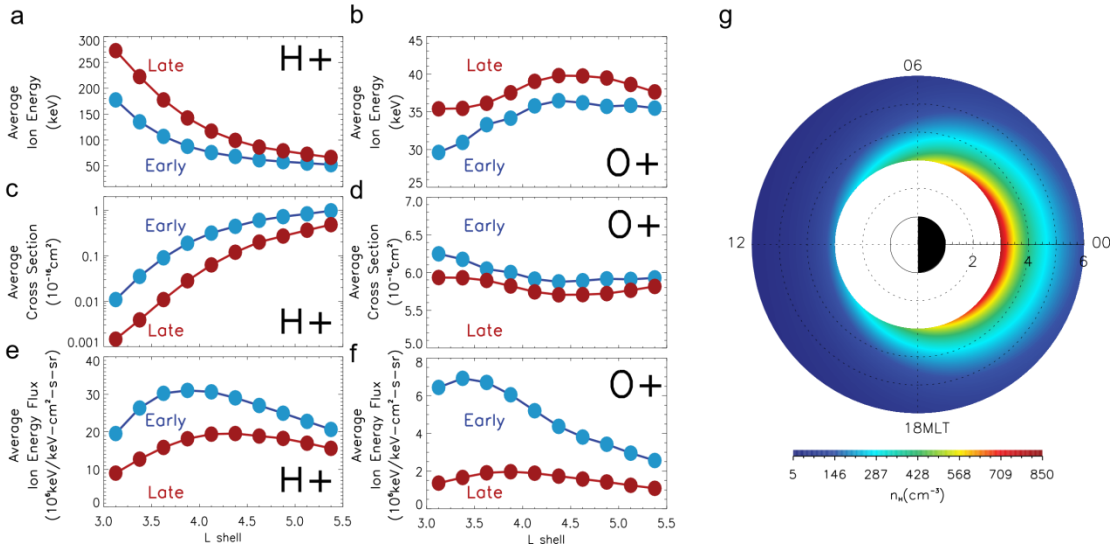

299

300 **Figure 4.** (a), (b) Average ion energy as a function of L shell ($\Delta L = 0.25$) for H^+ and O^+.
301 (c), (d) Average charge exchange cross-section as a function of L shell ($\Delta L = 0.25$) for
302 H^+ and O^+. Cross-sections are calculated by Lindsay and Stebbings (2005). (e), (f)
303 Average ion energy flux as a function of L shell ($\Delta L = 0.25$) for H^+ and O^+. Results
304 during early (late) recovery phases are indicated by blue (red) points. (g) The spatial
305 distribution of exospheric hydrogen density, calculated using the model of Cson Brandt
306 et al. (2002) and Rairden et al. (1986).

307

308 # Appendix

309 **Correction of spacecraft spatial variations.** This correction was included to remove
310 the influence of orbital displacement (primarily in the L shell direction) on energy
311 density variations at observed positions. We first calculated the average energy density
312 using RBSP data (from 2013–2016) under four different conditions: SYM-H<−50 nT,
313 −50 nT <SYM-H<−30 nT, −30 nT <SYM-H<−10 nT and SYM-H>−10 nT. We then
314 calculated the change in average energy density with L shell using calibration curves
315 with a resolution of 0.001 L. These curves are shown for four different conditions in

Appendix Figure 1. Specific correction steps were as follows: (1) the observed point was assumed to be on the linear fit line and was extended 15s forward and backward to calculate the change in energy density based on the linear fit. This variation is considered as the change in energy density over 30 seconds. (2) The energy density in this 30-second window was corrected at the observed point using the calibration curves discussed above. Curves were subtracted from the change in energy density only if the change in L shell exceeded 0.001 in the 30-second window. (3) The decrease in energy density was divided by the interval time (30 s) to produce a local ring current energy density decease rate at the observed point.

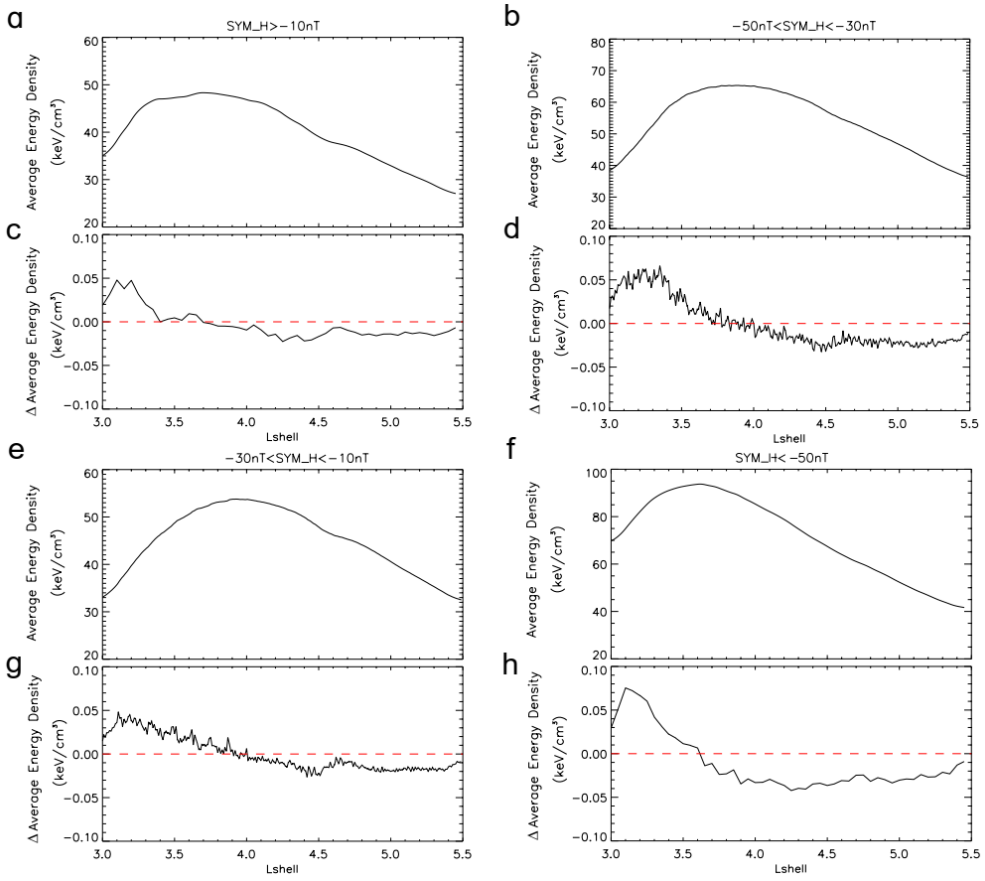

Appendix Figure 1. (a), (b), (e), (f) Average energy density as a function of L shell ($\Delta L = 0.05$) under four different geomagnetic conditions. (c), (d), (g), (h) The

corresponding calibration curves under four different geomagnetic conditions.

Acknowledgments. This work was supported by the Strategic Priority Research Program of the Chinese Academy of Sciences (Grant No. XDB41010304), Beijing Municipal Science and Technology Commission (Grant No. Z191100004319001), the National Natural Science Foundation of China (41874080, 41874197), and the China Scholarship Council (award to S.Y. Li for 1 year study abroad at Ludwig Maximilians University Munich). EK is supported by the German Research Foundation (DFG) under KR 4375/2-1 within SPP "Dynamic Earth." We acknowledge the use of RBSPICE and HOPE flux data acquired onboard the Van Allen probes (https://spdf.gsfc.nasa.gov/pub/data/rbsp/). SYM-H data originated from OMNIWeb (https://omniweb.gsfc.nasa.gov/form/omni_min.html).

References

Bailey, J., & Gruntman, M. (2011). Experimental Study of Exospheric Hydrogen Atom Distributions by Lyman-Alpha Detectors on the Twins Mission. Journal of Geophysical Research: Space Physics, 116. http://doi.org/10.1029/2011ja016531

Cheng, A. F. (1986). Energetic Neutral Particles from Jupiter and Saturn. Journal of Geophysical Research: Space Physics, 91(A4), 4524-4530. https://doi.org/10.1029/JA091iA04p04524

Cson Brandt, P., Demajistre, R., Roelof, E. C., Ohtani, S., Mitchell, D. G., & Mende, S. (2002). Image/High-Energy Energetic Neutral Atom: Global Energetic Neutral Atom Imaging of the Plasma Sheet and Ring Current During Substorms. Journal of Geophysical Research: Space Physics, 107(A12), SMP 21-21-SMP 21-13. http://doi.org/10.1029/2002ja009307

Daglis, I. A., & Kozyra, J. U. (2002). Outstanding Issues of Ring Current Dynamics. Journal of Atmospheric and Solar-Terrestrial Physics, 64(2), 253-264. http://doi.org/10.1016/s1364-6826(01)00087-6

Daglis, I. A., Kozyra, J. U., Kamide, Y., Vassiliadis, D., Sharma, A. S., Liemohn, M. W.,

et al. (2003). Intense Space Storms: Critical Issues and Open Disputes. Journal of Geophysical Research-Space Physics, 108(A5). http://doi.org/10.1029/2002ja009722

Daglis, I. A., Thorne, R. M., Baumjohann, W., & Orsini, S. (1999). The Terrestrial Ring Current: Origin, Formation, and Decay. Reviews of Geophysics, 37(4), 407-438. http://doi.org/10.1029/1999rg900009

Ebihara, Y., & Ejiri, M. (2000). Simulation Study on Fundamental Properties of the Storm-Time Ring Current. Journal of Geophysical Research-Space Physics, 105(A7), 15843-15859. http://doi.org/10.1029/1999ja900493

Ebihara, Y., Fok, M. C., Immel, T. J., & Brandt, P. C. (2011). Rapid Decay of Storm Time Ring Current Due to Pitch Angle Scattering in Curved Field Line. Journal of Geophysical Research-Space Physics, 116(A3). http://doi.org/10.1029/2010ja016000

Fahr, H.-J., Fichtner, H., & Scherer, K. (2007). Theoretical Aspects of Energetic Neutral Atoms as Messengers from Distant Plasma Sites with Emphasis on the Heliosphere. Reviews of Geophysics, 45(4). http://doi.org/10.1029/2006rg000214

Fok, M.-C., Moore, T. E., & Greenspan, M. E. (1996). Ring Current Development During Storm Main Phase. Journal of Geophysical Research: Space Physics, 101(A7), 15311-15322. http://doi.org/10.1029/96ja01274

Fok, M.-C., Moore, T. E., Kozyra, J. U., Ho, G. C., & Hamilton, D. C. (1995). Three-Dimensional Ring Current Decay Model. Journal of Geophysical Research, 100(A6), 9619. http://doi.org/10.1029/94ja03029

Fok, M. C., Kozyra, J. U., Nagy, A. F., Rasmussen, C. E., & Khazanov, G. V. (1993). Decay of Equatorial Ring Current Ions and Associated Aeronomical Consequences. Journal of Geophysical Research: Space Physics, 98(A11), 19381-19393. http://doi.org/10.1029/93ja01848

Funsten, H. O., Skoug, R. M., Guthrie, A. A., MacDonald, E. A., Baldonado, J. R., Harper, R. W., et al. (2013). Helium, Oxygen, Proton, and Electron (Hope) Mass Spectrometer for the Radiation Belt Storm Probes Mission. Space Science Reviews, 179(1-4), 423-484. http://doi.org/10.1007/s11214-013-9968-7

Gonzalez, W. D., Joselyn, J. A., Kamide, Y., Kroehl, H. W., Rostoker, G., Tsurutani, B. T., & Vasyliunas, V. M. (1994). What Is a Geomagnetic Storm? Journal of Geophysical Research, 99(A4), 5771. http://doi.org/10.1029/93ja02867

Hamilton, D. C., Gloeckler, G., Ipavich, F. M., Stüdemann, W., Wilken, B., & Kremser, G. (1988). Ring Current Development During the Great Geomagnetic Storm of February 1986. Journal of Geophysical Research, 93(A12), 14343. http://doi.org/10.1029/JA093iA12p14343

Ilie, R., Skoug, R. M., Funsten, H. O., Liemohn, M. W., Bailey, J. J., & Gruntman, M. (2013). The Impact of Geocoronal Density on Ring Current Development. Journal of Atmospheric and Solar-Terrestrial Physics, 99, 92-103. http://doi.org/10.1016/j.jastp.2012.03.010

Jordanova, V. K., Miyoshi, Y. S., Zaharia, S., Thomsen, M. F., Reeves, G. D., Evans, D. S., et al. (2006). Kinetic Simulations of Ring Current Evolution During the

Geospace Environment Modeling Challenge Events. Journal of Geophysical Research, 111(A11). http://doi.org/10.1029/2006ja011644

Jorgensen, A. M., Henderson, M. G., Roelof, E. C., Reeves, G. D., & Spence, H. E. (2001). Charge Exchange Contribution to the Decay of the Ring Current, Measured by Energetic Neutral Atoms (Enas). Journal of Geophysical Research: Space Physics, 106(A2), 1931-1937. http://doi.org/10.1029/2000ja000124

Keika, K., Brandt, P. C., Nosé, M., & Mitchell, D. G. (2011). Evolution of Ring Current Ion Energy Spectra During the Storm Recovery Phase: Implication for Dominant Ion Loss Processes. Journal of Geophysical Research: Space Physics, 116(A5). http://doi.org/10.1029/2010ja015628

Keika, K., Nosé, M., Brandt, P. C., Ohtani, S., Mitchell, D. G., & Roelof, E. C. (2006). Contribution of Charge Exchange Loss to the Storm Time Ring Current Decay: Image/Hena Observations. Journal of Geophysical Research, 111(A11). http://doi.org/10.1029/2006ja011789

Keika, K., Nosé, M., Ohtani, S., Takahashi, K., Christon, S. P., & McEntire, R. W. (2005). Outflow of Energetic Ions from the Magnetosphere and Its Contribution to the Decay of the Storm Time Ring Current. Journal of Geophysical Research: Space Physics, 110(A9). http://doi.org/10.1029/2004ja010970

Le, G., Russell, C. T., & Takahashi, K. (2004). Morphology of the Ring Current Derived from Magnetic Field Observations. Annales Geophysicae, 22(4), 1267-1295. http://doi.org/10.5194/angeo-22-1267-2004

Liemohn, M. W., Kozyra, J. U., Thomsen, M. F., Roeder, J. L., Lu, G., Borovsky, J. E., & Cayton, T. E. (2001). Dominant Role of the Asymmetric Ring Current in Producing the Stormtimedst*. Journal of Geophysical Research: Space Physics, 106(A6), 10883-10904. http://doi.org/10.1029/2000ja000326

Lindsay, B. G., & Stebbings, R. F. (2005). Charge Transfer Cross Sections for Energetic Neutral Atom Data Analysis. Journal of Geophysical Research, 110(A12). http://doi.org/10.1029/2005ja011298

Louarn, P., Roux, A., Perraut, S., Kurth, W. S., & Gurnett, D. A. (2000). A Study of the Jovian “Energetic Magnetospheric Events” Observed by Galileo: Role in the Radial Plasma Transport. Journal of Geophysical Research: Space Physics, 105(A6), 13073-13088. http://doi.org/10.1029/1999ja900478

Mauk, B. H. (2004). Energetic Ion Characteristics and Neutral Gas Interactions in Jupiter's Magnetosphere. Journal of Geophysical Research, 109(A9). http://doi.org/10.1029/2003ja010270

Mauk, B. H. (2020). Chapter 9 - Comparative Planetary Ring Currents. In Jordanova, Ilie, & Chen (Eds.), Ring Current Investigations (pp. 271-307): Elsevier.

Mauk, B. H., Mitchell, D. G., Krimigis, S. M., Roelof, E. C., & Paranicas, C. P. (2003). Energetic Neutral Atoms from a Trans-Europa Gas Torus at Jupiter. Nature, 421(6926), 920-922. http://doi.org/10.1038/nature01431

Mauk, B. H., Saur, J., Mitchell, D. G., Roelof, E. C., Brandt, P. C., Armstrong, T. P., et al. (2005). Energetic Particle Injections in Saturn's Magnetosphere. Geophysical Research Letters, 32(14). http://doi.org/10.1029/2005gl022485

Mauk, B. H., Williams, D. J., McEntire, R. W., Khurana, K. K., & Roederer, J. G.

(1999). Storm-Like Dynamics of Jupiter's Inner and Middle Magnetosphere. Journal of Geophysical Research: Space Physics, 104(A10), 22759-22778. http://doi.org/10.1029/1999ja900097

McEntire, R. W., Lui, A. T. Y., Krimigis, S. M., & Keath, E. P. (1985). Ampte/Cce Energetic Particle Composition Measurements During the September 4, 1984 Magnetic Storm. Geophysical Research Letters, 12(5), 317-320. http://doi.org/10.1029/GL012i005p00317

Mitchell, D. G., Lanzerotti, L. J., Kim, C. K., Stokes, M., Ho, G., Cooper, S., et al. (2014). Radiation Belt Storm Probes Ion Composition Experiment (Rbspice). In Fox & Burch (Eds.), The Van Allen Probes Mission (pp. 263-308). Boston, MA: Springer US.

Østgaard, N. (2003). Neutral Hydrogen Density Profiles Derived from Geocoronal Imaging. Journal of Geophysical Research, 108(A7). http://doi.org/10.1029/2002ja009749

Rairden, R. L., Frank, L. A., & Craven, J. D. (1986). Geocoronal Imaging with Dynamics Explorer. Journal of Geophysical Research, 91(A12), 13613. http://doi.org/10.1029/JA091iA12p13613

Sergis, N., Bunce, E. J., Carbary, J. F., Cowley, S. W. H., Jia, X., Hamilton, D. C., et al. (2018). The Ring Current of Saturn. In Electric Currents in Geospace and Beyond (pp. 139-154).

Smith, H. T., Mitchell, D. G., Johnson, R. E., Mauk, B. H., & Smith, J. E. (2019). Europa Neutral Torus Confirmation and Characterization Based on Observations and Modeling. The Astrophysical Journal, 871(1), 69. http://doi.org/10.3847/1538-4357/aaed38

Wing, S., Brandt, P. C., Mitchell, D. G., Johnson, J. R., Kurth, W. S., & Menietti, J. D. (2020). Periodic Narrowband Radio Wave Emissions and Inward Plasma Transport at Saturn's Magnetosphere. The Astronomical Journal, 159(6), 249. http://doi.org/10.3847/1538-3881/ab818d

Young, S. L., Denton, R. E., Anderson, B. J., & Hudson, M. K. (2008). Magnetic Field Line Curvature Induced Pitch Angle Diffusion in the Inner Magnetosphere. Journal of Geophysical Research: Space Physics, 113(A3), n/a-n/a. http://doi.org/10.1029/2006ja012133

Zoennchen, J. H., Nass, U., Lay, G., & Fahr, H. J. (2010). 3-D-Geocoronal Hydrogen Density Derived from Twins Ly-A-Data. Annales Geophysicae, 28(6), 1221-1228. http://doi.org/10.5194/angeo-28-1221-2010

Figure.

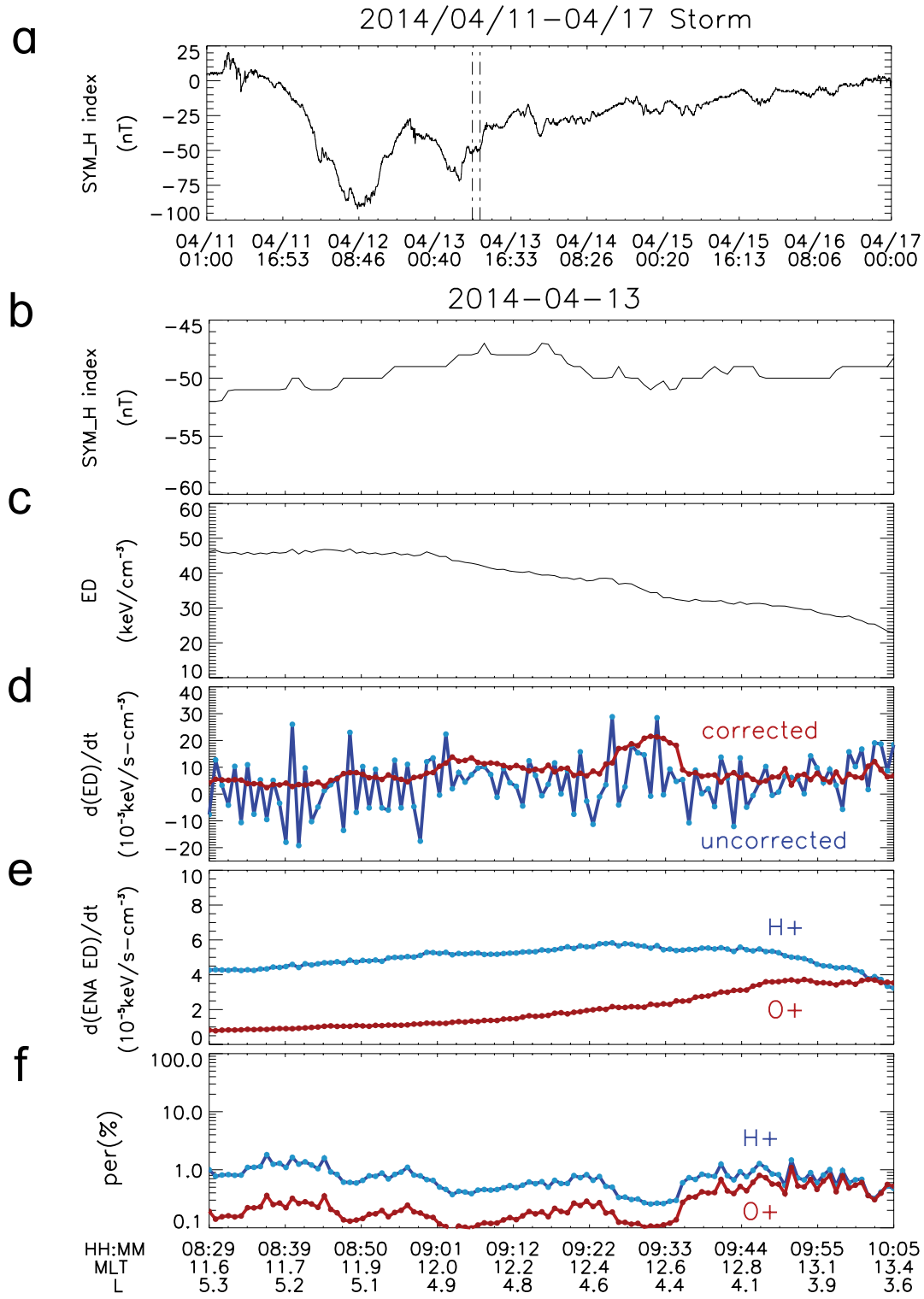
a
2014/04/11–04/17 Storm
SYM_H index (nT)
25
0
−25
−50
−75
−100
04/11 01:00
04/11 16:53
04/12 08:46
04/13 00:40
04/13 16:33
04/14 08:26
04/15 00:20
04/15 16:13
04/16 08:06
04/17 00:00
b
2014–04–13
SYM_H index (nT)
−45
−50
−55
−60
c
ED (keV/cm⁻³)
60
50
40
30
20
10
d
d(ED)/dt (10⁻³keV/s–cm⁻³)
40
30
20
10
0
−10
−20
corrected
uncorrected
e
d(ENA ED)/dt (10⁻³keV/s–cm⁻³)
10
8
6
4
2
0
H+
O+
f
per(%)
100.0
10.0
1.0
0.1
H+
O+
HH:MM
MLT
L
08:29 11.6 5.3
08:39 11.7 5.2
08:50 11.9 5.1
09:01 12.0 4.9
09:12 12.2 4.8
09:22 12.4 4.6
09:33 12.6 4.4
09:44 12.8 4.1
09:55 13.1 3.9
10:05 13.4 3.6

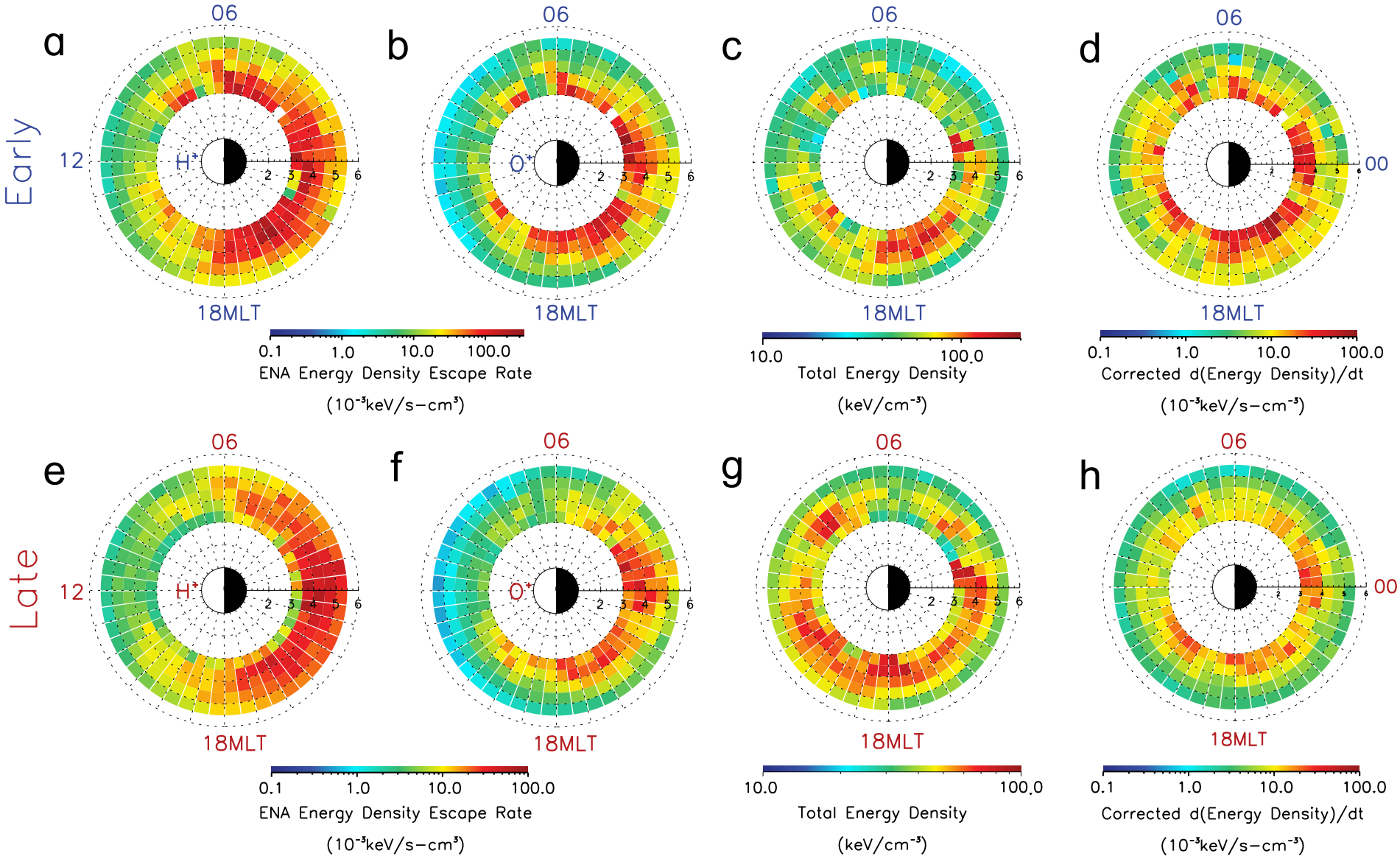
a
b
c
d
e
f
g
h
Early
Late
06
12
00
18MLT
H+
O+
0.1
1.0
10.0
100.0
ENA Energy Density Escape Rate
(10⁻³keV/s−cm³)
10.0
100.0
Total Energy Density
(keV/cm⁻³)
Corrected d(Energy Density)/dt
(10⁻³keV/s−cm⁻³)

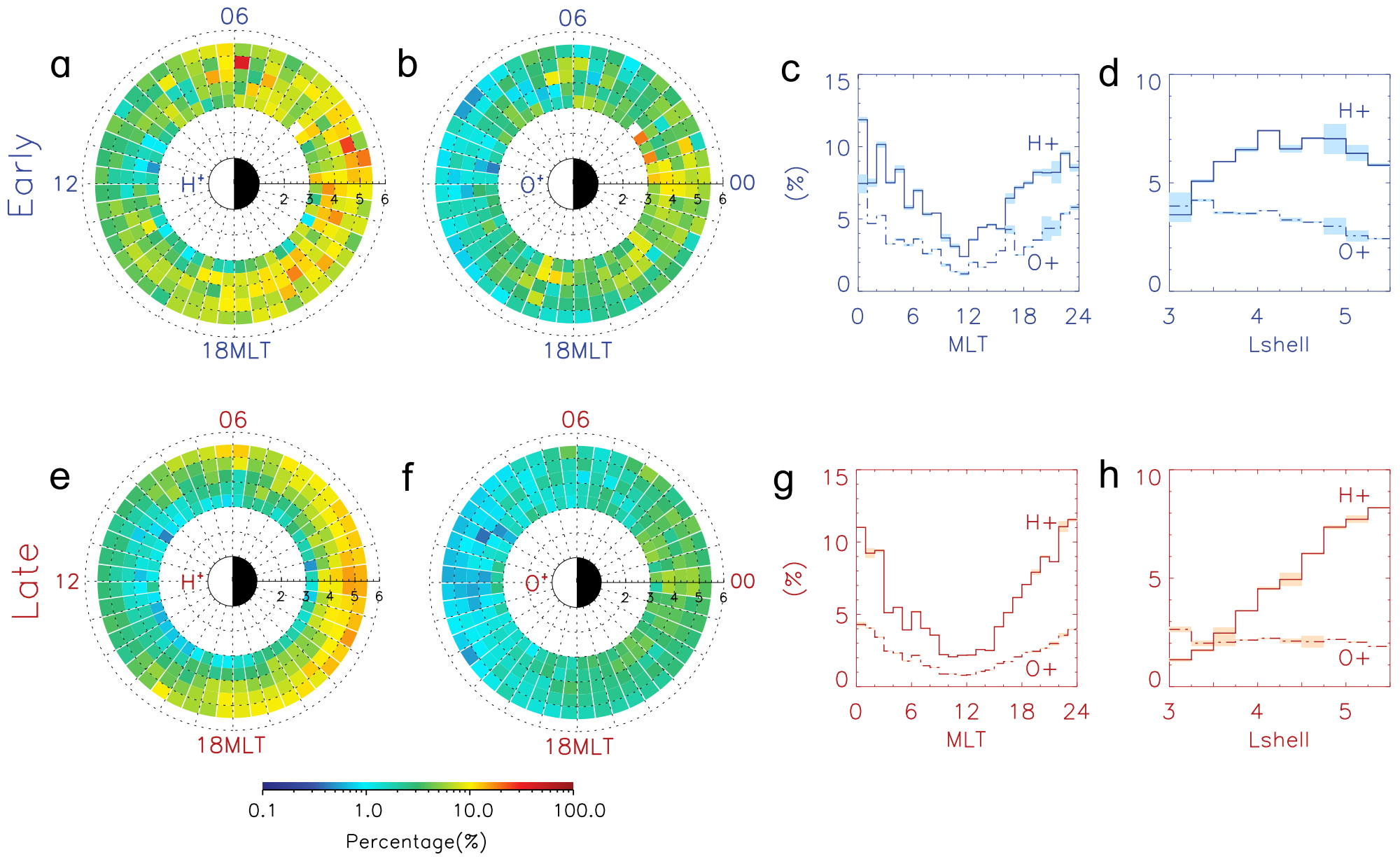
a
b
c
d
e
f
g
h
Early
Late
06
12
00
18MLT
H+
O+
2
3
4
5
6
(%)
MLT
Lshell
0.1
1.0
10.0
100.0
Percentage(%)

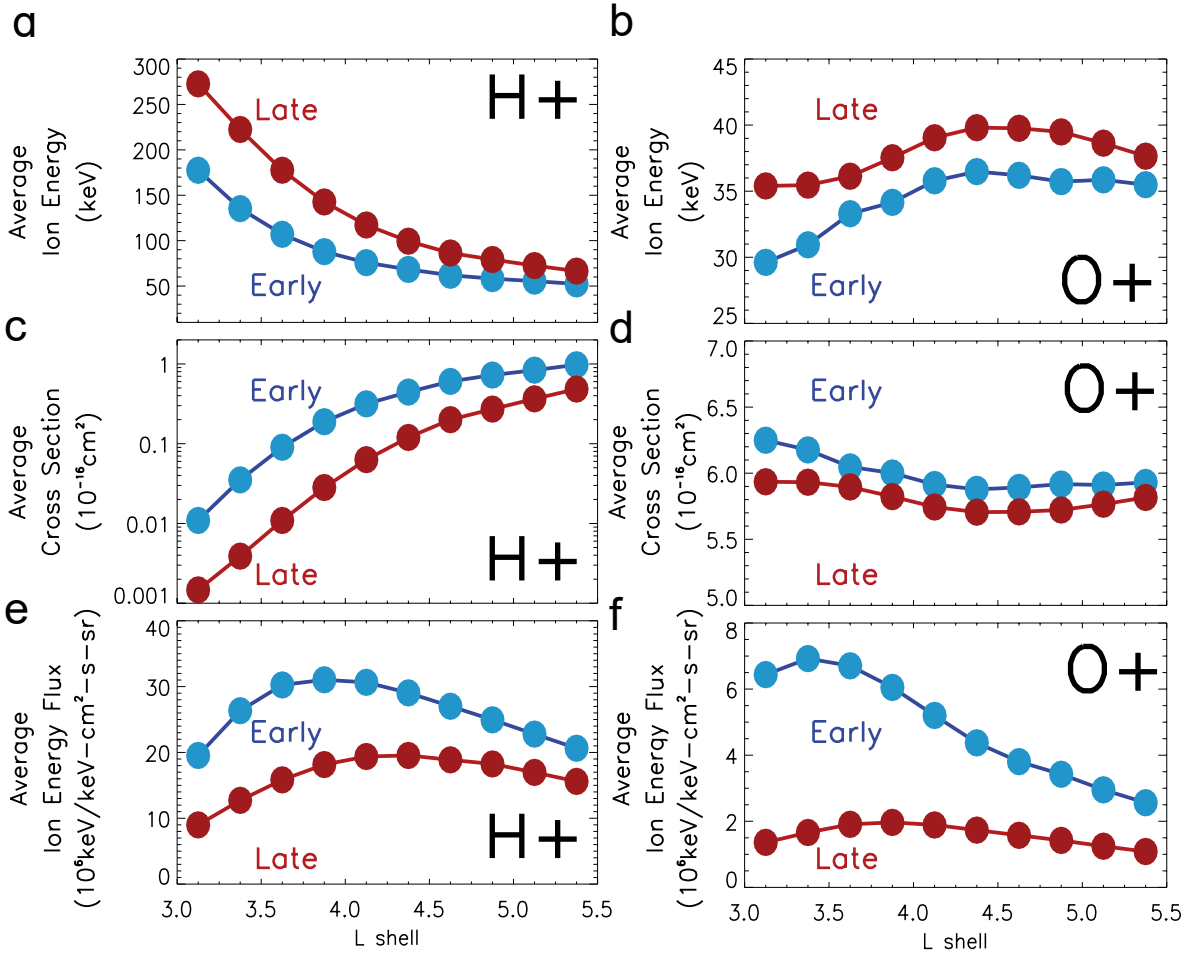
a
b
c
d
e
f
Late
Early
H+
O+
Average Ion Energy (keV)
Average Cross Section (10^{-16}cm^2)
Average Ion Energy Flux (10^6keV/keV-cm^2-s-sr)
L shell

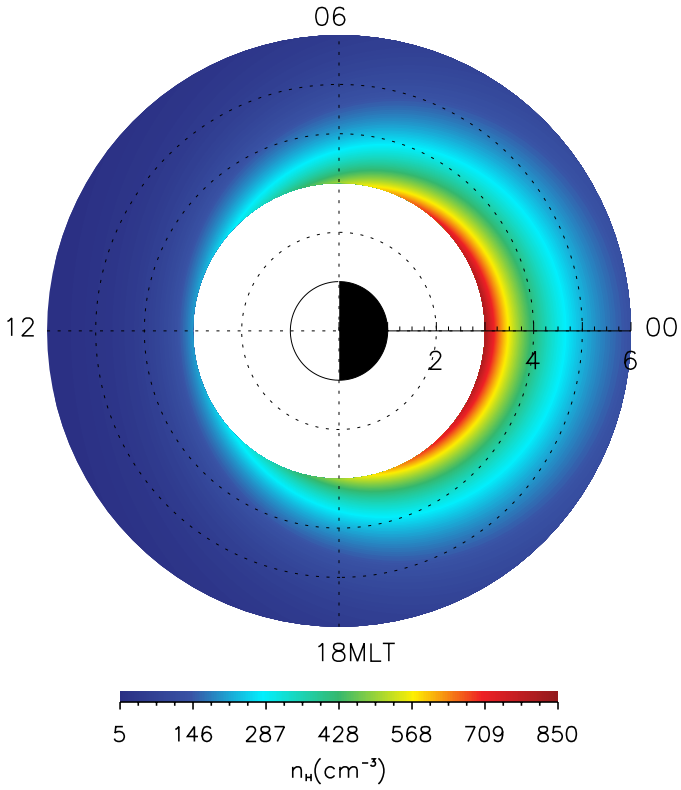
g
06
12
00
18MLT
2
4
6
5
146
287
428
568
709
850
n_H(cm^{-3})

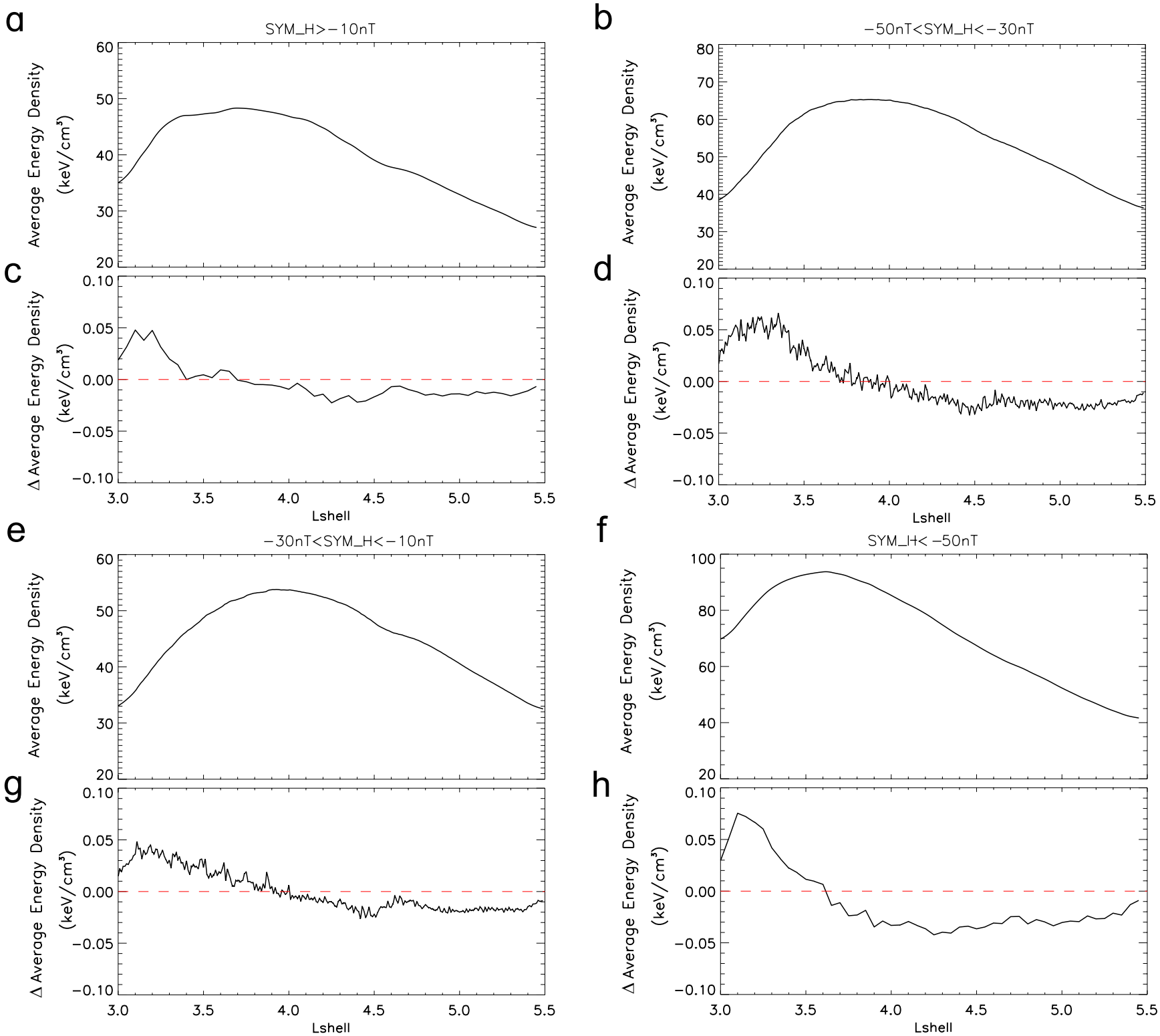
a
SYM_H>−10nT
Average Energy Density (keV/cm³)
b
−50nT<SYM_H<−30nT
Average Energy Density (keV/cm³)
c
Δ Average Energy Density (keV/cm³)
Lshell
d
Δ Average Energy Density (keV/cm³)
Lshell
e
−30nT<SYM_H<−10nT
Average Energy Density (keV/cm³)
f
SYM_H< −50nT
Average Energy Density (keV/cm³)
g
Δ Average Energy Density (keV/cm³)
Lshell
h
Δ Average Energy Density (keV/cm³)
Lshell